The final publication is available at

https://doi.org/10.1016/j.ssi.2021.115851

Additional Information

Reversible electrodes based on B-site substituted $Ba_{0.5}Sr_{0.5}Co_{0.8}Fe_{0.2}O_{3-\delta}$ for intermediate temperature solid-oxide cells

L. Navarrete[1], C. Hannahan[1] and J.M. Serra[1]*

[1]Instituto de Tecnología Química (Universitat Politècnica de València – Consejo Superior de Investigaciones Científicas), Av. Los Naranjos, s/n, 46022 Valencia, Spain

Abstract

The $Ba_{0.5}Sr_{0.5}Co_{0.8}Fe_{0.2}O_{3-\delta}$ perovskite is a promising electrode material for solid-oxide cells electrochemical cells exhibiting excellent oxygen reduction reaction (ORR) activity and mixed ionic-electronic transport properties at intermediate temperatures but suffers from stability issues. In this work, the effect on stability and electrochemical performance of several B-site substituted cations (Sc, Zr, Y) are studied. The presence of these substituted cations improved stability by preventing (a) the formation of the detrimental hexagonal phase during long term air exposure experiments and (b) reducing the formation of carbonates in CO_2-containing atmospheres. Symmetrical cell testing revealed that the Sc-substituted material mixed with an ionic gadolinium-doped ceria (GDC) phase has the lowest polarization among the materials and thus was chosen as the cathode for the full cell construction. The composite electrode achieved encouraging power density values ~877 mW/cm^2 at 700 °C. The material showed stable hydrogen generation during intermediate temperature electrolysis tests and its performance improved upon the introduction of CO_2 to carry out co-electrolysis. Furthermore, methane was obtained during co-electrolysis and Sabatier reaction at temperatures below 450 °C. The superior stability and performance of the Sc-substituted $Ba_{0.5}Sr_{0.5}Co_{0.8}Fe_{0.2}O_{3-\delta}$ make it an exciting candidate for application as a cathode in reduced temperature electrochemical cells.

Keywords

Co-electrolysis, reversible, fuel cell, stability, methane, cathode.

1. Introduction

Presently, the majority of the world's energy comes from fossil fuel sources such as coal, oil and natural gas resulting in the emission of greenhouse gases (GHG). The most prevalent GHG is CO_2 and it accounts for more than 50% of industrial emissions with 33

Gt having been released into the atmosphere in 2019 [1]. Transitioning away from CO_2 producing technologies will require the support of renewable energy sources. However, production from renewable technologies like wind turbines and solar panels fluctuates greatly depending on the time of day or weather patterns. To overcome this intermittency and create a stable renewable grid, the world's energy storage capacity must be massively increased. Hydrogen can be a key tool for energy storage as it is a flexible energy carrier which can be utilized by fuel cells to produce electricity. Furthermore, it is an important feedstock in many important industrial processes. Although H_2 is abundant in nature, hydrogen production today is very energy intensive. The most conventional methods for H_2 production are steam reforming, coal gasification or partial oxidation of heavy hydrocarbons. These traditional techniques use a fossil fuel feedstock leading to CO_2 generation. On the other hand, producing H_2 from water via electrolysis is less energetically demanding and does not result in GHG emissions.

In recent years, great efforts have been focused towards improving the fuel cells used to convert green hydrogen into electricity. One of these efforts is the search for novel materials to be used as cathodes for fuel cells in the intermediate temperature range (IT-SOFC). The cathodes used presently suffer from poor oxygen reduction reaction (ORR) activity at these temperatures (<700 °C) which limits the fuel cell performance. Mixed ionic electronic conducting (MIEC) materials have attracted great interest due to their potential as efficient IT-SOFC cathodes. The dual conductivity provided by an MIEC extends the triple phase boundary (TPB) such that it exists along the entire electrode. Among MIEC materials, ABO3 perovskite compounds possess attractive qualities and have been extensively studied for fuel cell and oxygen permeation applications [2–4]. A versatile family of compounds with interesting properties can be derived from the ABO3 framework by incorporating different cations into the lattice structure. For example, the partial substitution of the A-site trivalent cations with divalent cations can generate oxygen vacancies leading to increased ionic conductivity or replacing the B-site ions with multivalent metal compounds can improve electronic conductivity [5]. One ABO3 perovskite which is particularly promising is $SrCo_{0.8}Fe_{0.2}O_{3-\delta}$ (SCF). The material's exceptional catalytic activity, high oxygen permeability and mixed ionic-electronic conductivity make it an attractive candidate for oxygen transport applications [6]. However, at low oxygen partial pressures and operation temperatures the SCF undergoes a transition from the cubic perovskite phase to that of brownmillerite. The resulting

crystal structure possesses lower oxygen conductivity than the original perovskite material, possibly due to the rearrangement of the oxygen vacancies within the structure [7]. Using the cationic substitution strategy, Sr can be partially replaced with Ba to suppress the formation of the brownmillerite phase while also increasing stability and permeation. The barium substitution in SCF results in the formation of $Ba_{0.5}Sr_{0.5}Co_{0.8}Fe_{0.2}O_{3-\delta}$ which is an exciting MIEC perovskite material with high transport rates and potential application as oxygen permeation membranes or as IT-SOFC cathodes [2,8]. One issue limiting BSCF's application is its instability in CO_2 containing atmospheres below 800°C. In these environments, the perovskite material interacts with carbon dioxide resulting in the formation of performance reducing carbonates [9,10]. In this work, cations with fixed valence and similar ionic radii were incorporated into the perovskite's B-site to create a compound with greater stability. The $Ba_{0.5}Sr_{0.5}(Co_{0.8}Fe_{0.2})_{0.97}B_{0.03}O_{3-\delta}$ (B=Sc,Zr,Y) compounds were prepared via the SSR method and the subsequent effects of the different cations was studied (Table 1).

Ion	Coordination	Oxidation state	Radius (Å)	
			LS	HS
Co	6	+2	0.65	0.745
Co	6	+3	0.545	0.61
Co	6	+4	-	0.53
Fe	6	+2	0.61	0.78
Fe	6	+3	0.55	0.645
Fe	6	+4	0.725	
Sc	6	+3	0.72	
Y	6	+3	0.9	
Zr	6	+4	0.745	

Table 1. Ionic radii of B cations for the different oxidation states and Spin States [11].

2. Methodology

$Ba_{0.5}Sr_{0.5}(Co_{0.8}Fe_{0.2})_{0.97}B_{0.03}O_{3-\delta}$ (B= Sc, Zr and Y) materials were prepared following the solid-state reaction method. The stoichiometric amounts of the precursor oxides and carbonates were ball milled such that small and uniform particles were obtained with maximum surface contact. The powder was formed into pellets by uniaxial pressing and then several hours of heating at 1150 °C to assure the formation of the phase. Finally, and in order to obtain a low particle size and homogenous size distribution, the pellets broken with a mortar and pestle were ball milled with ZrO_2 balls in acetone.

The synthesized powders were characterized using X-ray diffraction analysis. The measurements were carried out in a PANalytical Cubix fast diffractometer by using $CuK\alpha1,2$ radiation, and an X'Celerator detector and Bruker D8 in Bragg-Brentano

geometry. XRD patterns were recorded in the 2θ range from 20 to 90 º and analyzed using the X'Pert HighScore Plus software.

Electrical conductivity measurements were carried out using the standard four-point DC technique on sintered rectangular bars. Powders of the different cathode materials were uniaxially pressed directly into rectangular bars and then fired at 1150 °C for 5 hours. Silver paste and wires were used to make the electric contacts. Measurements were performed in air and the current was supplied by a Keithley 2601 programmable current source. The voltage drop through the sample was detected by a Keithley 3706 multimeter.

The compatibility of a BSCF cathode with different electrolyte materials has been widely studied. When in contact with an yttrium stabilized zirconia (YSZ) electrolyte a reaction starts to occur at 800°C during the calcination step. By the time the temperature passes 950°C the BSCF is completely decomposed [12]. In order to ensure good electrode-electrolyte attachment and reduce interface resistance, annealing temperatures higher than 800 °C are required. Thus, a different electrolyte material must be selected to avoid the reaction with YSZ and the subsequent decomposition of the BSCF electrode. Gadolinia-doped ceria oxide ($Gd_{0.2}Ce_{0.8}O_{2-\delta}$, GDC) was selected as the electrolyte material in the symmetrical cell configuration for cathode characterization. GDC exhibits higher ionic conductivity and faster oxygen surface exchange kinetics than the zirconia-based electrolytes at intermediate temperatures [13], while no reaction is observed for the required electrode firing temperatures. Dense GDC electrolytes were prepared by uniaxial pressing of commercial powder (Treibacher) followed by impregnation with 5% of Co (with a solution of $CoN_2O_6 \cdot 6H_2O$). A final firing step was performed at 1480 °C to fully densify the electrolyte disks.

Another challenge related to cell construction is the delamination of the cathode from the electrolyte due to mismatched thermal expansion properties of the two materials. The thermal expansion coefficient (TEC) of BSCF is nearly 2 times bigger than the GDC [14]. To mitigate this problem, the BSCF materials were mixed with $Ce_{0.8}Gd_{0.2}O_{2-\delta}$ at a 50% weight ratio. Screen-printable inks were then prepared by mixing the composite powders with 6% wt. ethyl cellulose-terpineol solution in a 1:1 weight ratio. Ethyl Cellulose was provided by Sigma-Aldrich (Ref. 247499). The resulting pastes were screen printed on both sides of a ≈ 1 mm dense electrolyte (15 mm OD). Porous electrodes were obtained

after the calcination of the screen- printed layers at 950 °C for 2 h. A top screen-printed gold mesh was applied onto the electrodes to act as a current collector.

Symmetrical cells were tested by Electrochemical Impedance Spectroscopy (EIS), using a Solartron 1470E/1455 FRA with an AC potential of 20 mV and a frequency sweep from 0.03 Hz to 1MHz. The EIS measurements were performed at different operation temperatures (between 450 °C and 900 °C) and oxygen partial pressures. Post-mortem analysis of the symmetrical cells was done by Scanning Electron Microscopy (SEM) using a JEOL JSM6300 electron microscope. BSCF composite electrodes were tested in fuel cell and electrolysis modes, to this aim, the oxygen electrode was screen printed on top of a Ni-YSZ supported cell provided from Forschungszentrum Jülich.

3. Results
3.1. Structural characterization
3.1.1. XRD

X-Ray Diffraction (XRD) patterns were recorded of the as-prepared BSCF-substituted materials and are depicted in Figure 1(a). The materials are labelled as follows: $Ba_{0.5}Sr_{0.5}Co_{0.8}Fe_{0.2}O_{3-\delta}$ (BSCF), $Ba_{0.5}Sr_{0.5}(Co_{0.8}Fe_{0.2})_{0.97}Y_{0.03}O_{3-\delta}$ (BSCFY), $Ba_{0.5}Sr_{0.5}(Co_{0.8}Fe_{0.2})_{0.97}Sc_{0.03}O_{3-\delta}$ (BSCFS) and $Ba_{0.5}Sr_{0.5}(Co_{0.8}Fe_{0.2})_{0.97}Zr_{0.03}O_{3-\delta}$ (BSCFZ). The diffraction peaks can be assigned to the cubic perovskite phase with a space group of *Pm3m* [15,16] and no traces of other phases can be detected to the limit of the XRD equipment resolution. From this, it can be concluded that all cations are well incorporated in the structure.

The instability of BSCF after extended exposure to air at temperatures below 800 °C has been widely reported [15,17–19]. The instability of the cubic phase (*C*) causes a gradual shift to the hexagonal phase (H). The formation of this hexagonal phase reportedly takes place at the grain boundaries within the membrane leading to adverse effects on the oxygen equilibration kinetics [20]. The H-phase's poor crystal symmetry and low concentration of mobile oxygen vacancies are not conducive to oxygen transport [18]. The stability of the synthesized materials was assessed via a comparative study of the XRD patterns before and after two weeks of heat treatment in synthetic air at 750°C. Referring to Figure 1(b), new peaks which are associated with the hexagonal phase *P6₃/mmc* space group can be observed after the treatment. The superior stability of the

substituted compounds over the parent BSCF material is reflected in the lesser intensity of the hexagonal peaks. The influence of B-site cations on the electrochemical performance and oxygen permeation fluxes of BSCF based compounds has been investigated by other authors as well [21–24]. Based on this study and prior research it seems that B-site substitution leads to improved long-term stability of the cubic perovskite phase at intermediate temperatures [20,25].
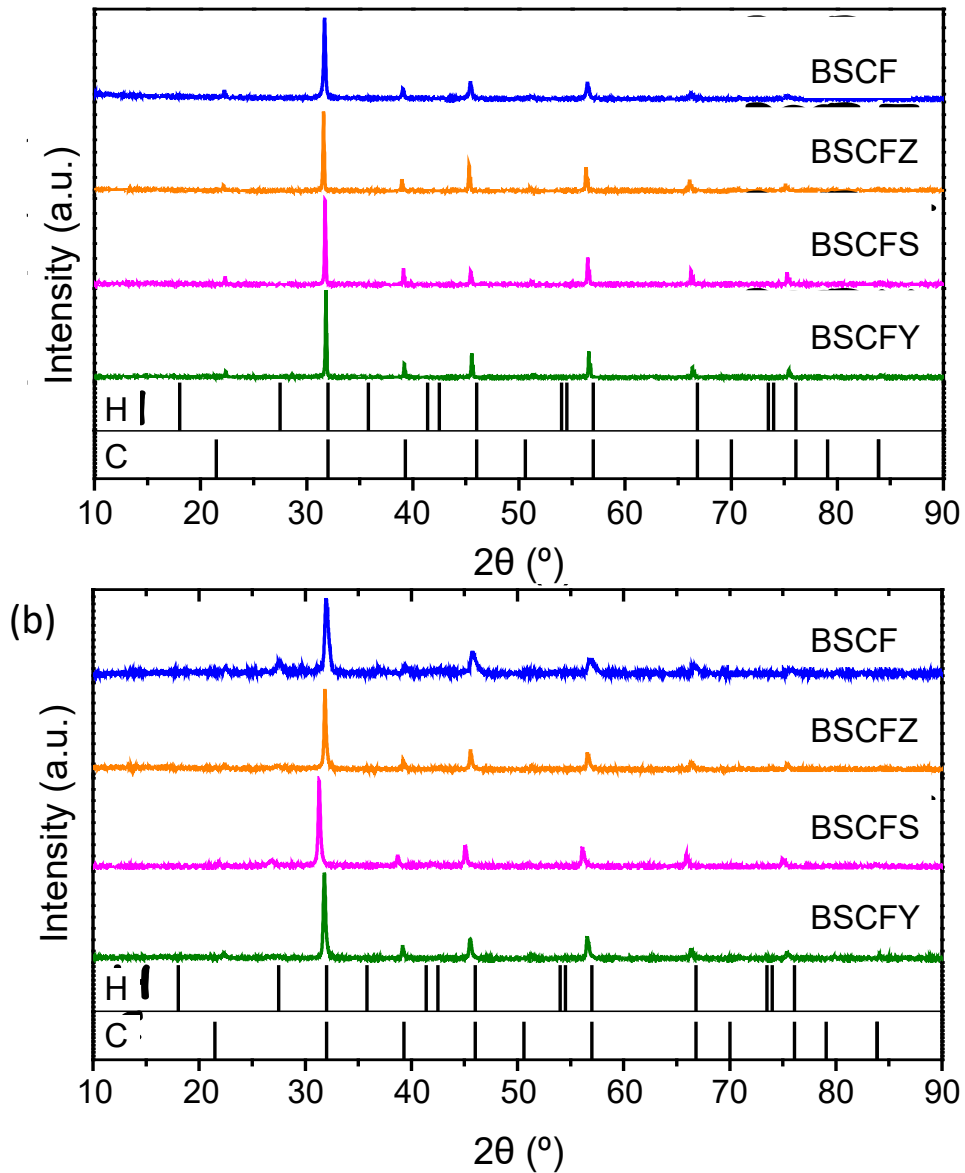

Figure 1. (a) XRD pattern of $Ba_{0.5}Sr_{0.5}(Co_{0.8}Fe_{0.2})_{0.97}B_{0.03}O_{3-\delta}$ (B= Sc, Zr and Y) as synthesized and (b) after stability test in air at 750 °C during two weeks. H and C correspond with hexagonal and cubic perovskite phases.
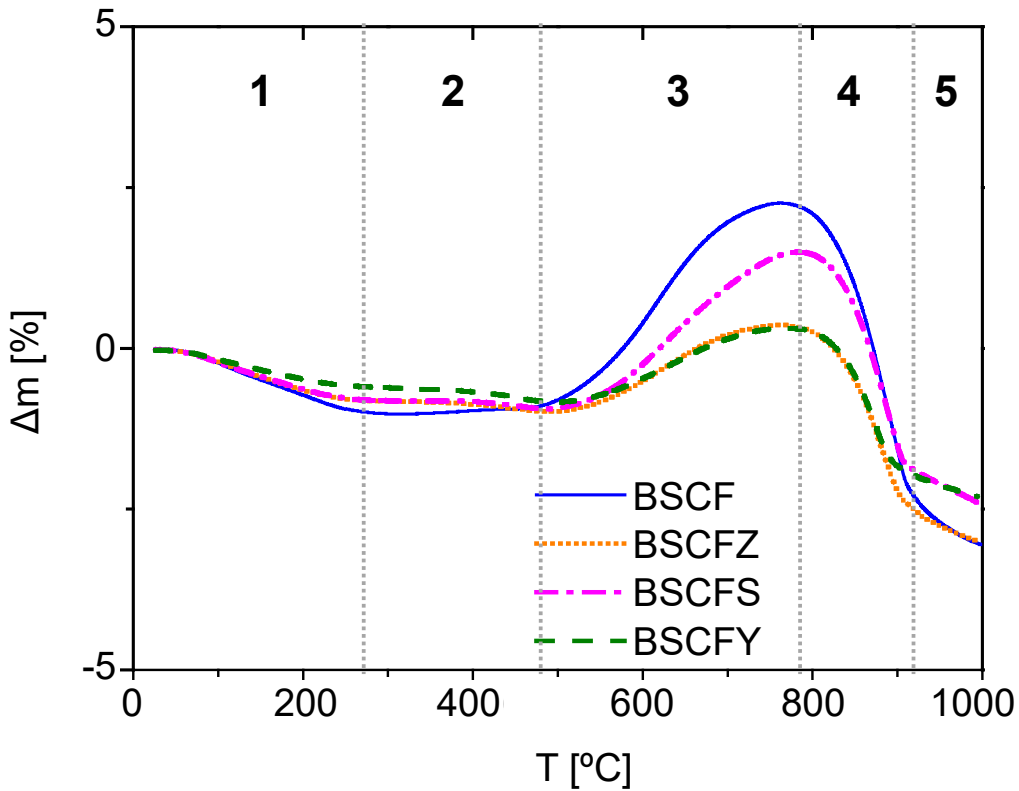
3.1.2. CO_2 stability

Figure 2. Thermogravimetric analysis of $Ba_{0.5}Sr_{0.5}(Co_{0.8}Fe_{0.2})_{0.97}B_{0.03}O_{3-\delta}$ *(B= Sc, Zr and Y)* in 5% CO_2/air atmosphere, Δm (mass change).

The instability of BSCF in presence of CO_2 has been widely reported [9,10], a thermogravimetric analysis of the different compounds according to temperature in a CO_2 containing atmosphere was performed. The results of the mass gain analysis for $Ba_{0.5}Sr_{0.5}(Co_{0.8}Fe_{0.2})_{0.97}B_{0.03}O_{3-\delta}$ (B= Sc, Zr and Y) series are presented in Figure 2. Five different regions can be distinguished:

- *Region 1* (RT-275 °C), there is a weight loss which can attributed to the material dehydration.
- *Region 2 (275 °C- 475 °C)*, the BSCF materials does not suffer any mass variation.
- *Region 3 (475 °C- 775 °C)*, at 475 °C there is an increase of the samples' weight until achieving a maximum. The temperature of the maximum varies as function of the compounds, being at 761.5, 762, 763.5, and 820.7 °C for the parent compound and Zr, Y and Sc substituted materials, respectively.
- *Region 4 (775 °C- 925 °C)*, carbonates produced in *Region 3* are decomposed when the temperature is increased above 800 °C [26].

- *Region 5 (925 °C-1000 °C)*, the high operation temperature forces the oxygen release and the vacancy formation and leads to a small loss of weight, in addition to the carbonates' decomposition.

According to the results obtained the substituted materials present higher stability in CO2 containing atmospheres, since higher temperatures are reached in the maximum of the different curves. Additionally, the percentage of the mass change for the substituted BSCF materials is smaller than the parent compound, indicating a lower carbonation level.

3.1.3. Total DC electrical conductivity

The electrical conductivity of the different compounds was measured using the four-point DC method on rectangular bars with a relative density > 95%. The results are presented in Figure 3. The incorporation of Sc (+3) into the BSCF structure led to an increase in conductivity in the temperature range of 500 to 800 °C. In the case of the Y-substituted material, the incorporation of Y has little effect on the conductivity at temperatures above 600 °C. At lower temperatures, the conductivity of the BSFCY was superior to that of the parent structure due to the fixed oxidation state of Y (3+) which led to enhanced electronic conductivity in this temperature range. The lowest total conductivity obtained was by BSCFZ in the high temperature range (> 500 °C). This poor conductivity could be related to the high oxidation state of the Zr (+4), which necessitates a charge compensation in the crystal structure leading to a reduced number of oxygen vacancies and electron holes.

In addition to the tests performed in air, conductivity measurements were also carried out under atmospheres consisting of a range of oxygen partial pressures. The studied extent of pO_2 includes both oxidant and moderate atmospheres. The total conductivity results at two different temperatures, 600 and 800 °C, are plotted in Figure 3. As is evident in figure 3(b), the total conductivity is dependent on the oxygen partial pressure. The slope values (nT) of log (σ) vs. log (pO_2) for the different materials are displayed in Table 2. The relationship between the conductivity and oxygen partial pressure (1/4<nT<1/6) indicates p-type electronic conductivity for all of the substituted BSCF compounds. Furthermore, the total conductivity increases due to the electronic conductivity enhancement with pO_2, i.e. electron holes are created due to the oxygen vacancies occupancy [27,28].

$$\frac{1}{2}O_2\,(g) + V_O^{\cdot\cdot} \rightarrow O_O^x + 2h^{\cdot}$$
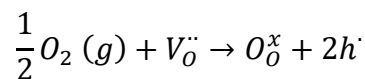
At low temperatures, the ionic conductivity is negligible, and p-type electronic conductivity dominates. However, at higher temperatures, oxygen is released from the structure causing the generation of oxygen vacancies and the elimination of electron holes leading to reduced electronic conductivity. (Table 2).

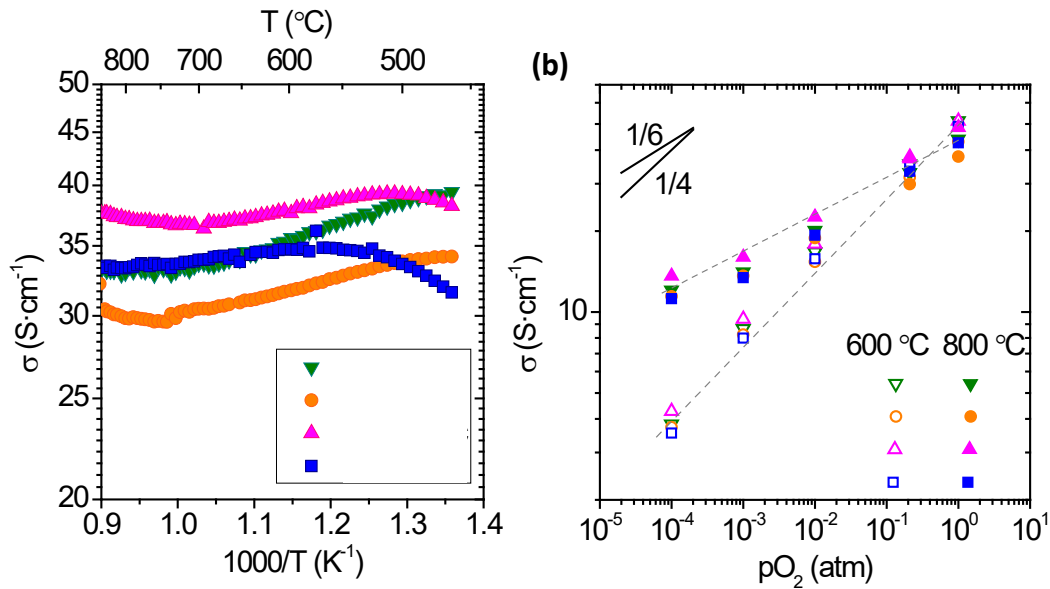|	600 ℃	800 ℃
BSFCY	0.27	0.14
BSFCZ	0.26	0.13
BSFCS	0.27	0.14
BSFC	0.28	0.15

Table 2. n values of log (σ) vs. log (pO2)

Figure 3. Total DC conductivity (a) as function of temperature in dry air and (b) as function of oxygen partial pressure.

3.1.4. Cathode testing on symmetric cells

Electrode polarization resistance (Rp) values were obtained by Electrochemical Impedance Spectroscopy of the symmetrical cells in the temperature range from 900 to 450 °C. The electrochemical performance of the different composite electrodes is presented in Figure 4 in an Arrhenius arrangement. Despite of the cation introduced in the cubic perovskite the electrode performance of the parent BSCF is improved at temperatures above 700 °C. However, at lower temperatures the Rp of BSCF, BSCFZ and BSCFY composites converge to a similar performance. Nevertheless, the BSCF substituted in B-site by Scandium reduces the polarization resistance in all temperature range.

At low temperatures BSCF is predominantly an electronic conductor with low ionic conductivity which leads to a lesser TPB zone. Therefore, the addition of an ionic phase such as GDC helps to create a composite electrode with a wider TPB and improved performance at low temperatures [29]. Below 750 °C the BSCF based electrodes show an increase in the activation energy. This inverse relationship between the activation energy and the operation temperatures could be ascribed to the change in conductivity of the composite material.

Electrode	Ea_1 [900-750 °C] (eV)	Ea_2 [750-450 °C] (eV)
BSFCY/GDC	0.50	0.81
BSFCZ/GDC	0.66	1.02
BSFCS/GDC	0.82	1.24
BSFC/GDC	0.63	0.96

Table 3. Activation energy of $Ba_{0.5}Sr_{0.5}(Co_{0.8}Fe_{0.2})_{0.97}B_{0.03}O_{3-\delta}$/GDC electrodes in synthetic air. Ea_1 related with high operation temperature and Ea_2 with low temperature.

The oxygen reduction reaction at the electrode is greatly influenced by the cations located in the B-site of the perovskite. Depending on its oxidation state, the cation can participate in redox cycles which favor the ORR. For example, the Co and Fe metal cations are both able to cycle between the 3+ and 4+ oxidation states allowing them to achieve low activation energies. On the other hand, Zr, Sc and Y have fixed oxidation states and do not participate in redox cycling leading to an increase of the Ea. Among the fixed state cations, the introduction of the 3+ Sc and Y leads to a lower ORR activation energy compared to for the higher charged Zr (4+). The higher activation energy attributed to the Zr may be due to the generation of oxygen vacancies which results from charge compensation in the BSCF phase by Sc and Zr incorporation. The same behavior can be observed in the total conductivity measurements i.e the higher conductivity of BSFCS and BSFCY over BSCF and BSFCY.
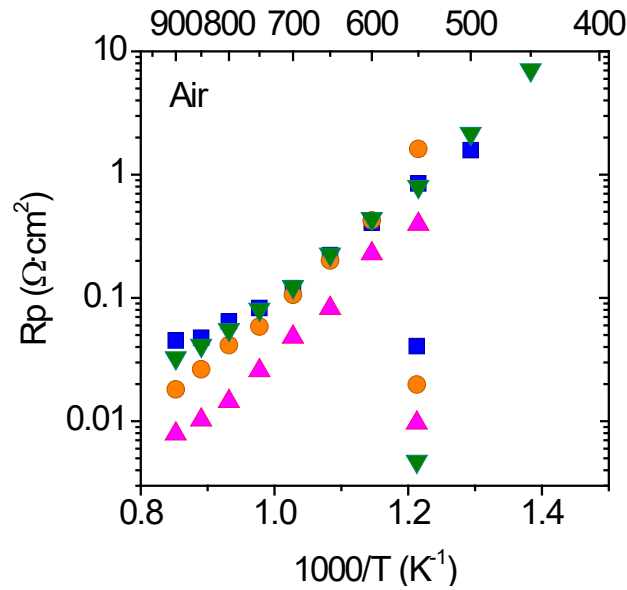
Figure 4. Electrode polarization resistance of BSCF-substituted-ceria-based composites in air as function of temperature.

Post-mortem cells were analyzed by Scanning Electron Microscopy (SEM), the cross-sectional micrographs of secondary electron detector display similar microstructures (Supporting information, S1). The larger particles are of the BSCF-substituted materials while the smaller ones make up the GDC phase. The observed porosity (> 35%, determined by the open software *ImageJ*) is sufficient for gas diffusion purposes.
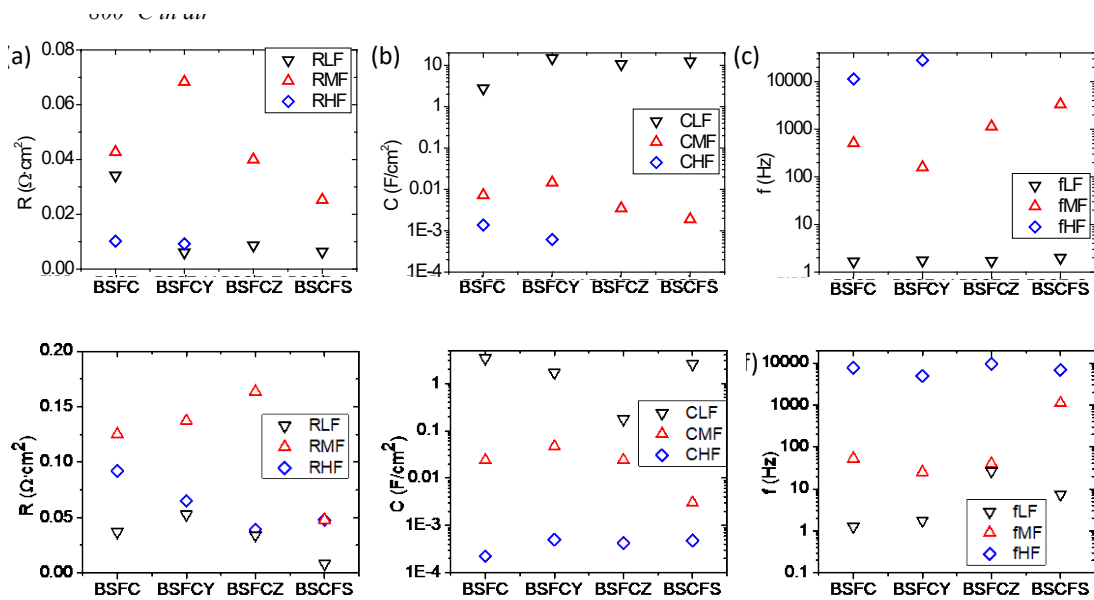

Figure 5. Equivalent electrical circuit fitting results; (a)/(d) resistance, (b)/(e) capacitance and (c)/(f) frequency of the different processes at 800 and 650 °C in air, for the composite electrodes. For clarification the results of the composite electrodes have been referred to the BSCF-substituted compound.

To further understand each cation's influence on the cathode performance, the EIS spectra have been fitted with an equivalent electrical circuit. Since two distinct activation energies

were observed in the Arrhenius plot, two different temperatures were selected to carry out the study, 800 °C and 650 °C. At the higher temperature, two equivalent circuits were chosen based on the number of limiting steps found in the EIS spectra. For example, the BSCFZ/GDC and BSCFS/GDC spectra consists of two arcs while those of BSCF/GDC and BSCFY/GDC contain three (Supporting information, S2), The Nyquist and Bode plots suggest that the limiting mechanism of the ORR takes place at low to medium frequencies. These frequencies are related to surface processes like O_2 incorporation into the bulk material and absorption and/or partial reduction of oxygen on the MIEC electrode [30].

The general equivalent formulated circuits consist of and inductance (L) and an ohmic resistance (R_Ω) component associated with the electrolyte conductivity, and two or three Constant Phase Elements (CPE) in parallel with a resistance. At 800 °C the two resistances limit the electrode performance: low (LF) and medium frequency (MF). However, at the lower temperature, the resistance associated with high frequency (HF) processes becomes more significant.

The LF resistance shows little variation in the frequency and associated capacitance, 1-10 Hz and 1-10 F/cm^2 respectively for both temperatures and for all the electrodes tested. Setevich *et al.* [23] reported the same behavior for the BSCF composite and suggested no dependence of this resistance on the microstructure of the electrode nor on a possible second phase formation during the electrode heat treatments. However, the LF resistance could be ascribed to surface processes such as the oxygen adsorption step ($O_2\ (g) \leftrightarrow O_{2,ads}$ and $O_{2,ads} \leftrightarrow 2O_{ads}$) [31–33].

As can be seen in Figure 6, the addition of all cation except Y reduces resistance at low to medium frequencies leading to improved electrode performance. At 800°C, the perovskite with 3% substitution of Zr or Y at the B-site exhibits lesser LF resistance which is ascribed to improved oxygen exchange (k_{chem}) and chemical diffusion coefficients (D_{chem}) [34,35]. However, at 650 °C the Y-substituted material shows higher LF resistance compared to the parent structure. This suggests that the presence of large Y cations distorts the perovskite structure having a negative effect on surface processes (Table 1). The Sc substituted electrode shows the least resistance at LF which reinforces

the hypothesized positive influence of small cation size and low oxidation state on oxygen adsorption.

The contribution of the HF regime at 10 kHz with an associated capacitance below $1 \cdot 10^{-3}$ F/cm^2 becomes predominant at lower temperatures. In high temperature environments, only BSCF and BSCFY exhibit HF resistance with a small contribution to the total Rp. However, as the temperature is lowered, the role of HF resistance becomes more significant. The effect is most pronounced in the Sc-substituted material in which the HF resistance is completely dominant. The impedance analysis values obtained here align with the results previously reported by Dusastre *et. al.,*[36] where the HF resistance originates from the O^{2-} transfer step at the electrode/electrolyte interface[37]. This can be attributed to the reduction in ionic conductivity of the GDC as the temperature is lowered [38], leading to a lesser TPB and diminished oxygen transfer to the electrolyte [39,40]. Likewise, the oxygen transport in the GDC phase itself is limited, worsening the cathode performance and the redox activity on the TPB.

At medium frequencies in the range of 100-1000 Hz with a capacitance of 0.001-0.1 F/cm^2 the generated arc is thermally activated [31] and its dependence on both microstructure and electrode configuration [31,41] implies that it is influenced by the TPB length. The MF resistance provides the greatest overall contribution to the total polarization resistance for all compounds throughout the temperature range. Since the microstructure deviates very little between the electrode materials, the MF resistance can be mostly attributed to the length of the TPB. At 800 °C the Y- substituted perovskite has the largest resistance which is probably due to a combination of cation size and oxygen incorporation into the perovskite bulk. On the other hand, at lower temperatures an RMF trend is observed which is similar to that of conductivity. It seems that the oxygen vacancies generated in the structure dominate the low temperature resistance. Therefore, each substituted material's capacity to form oxygen vacancies will be the difference maker. For example, the Zr substituted electrode exhibits the highest low temperature resistance which suggests that it's fixed +4 oxidation state requires a lower amount of oxygen vacancies to maintain the perovskite electroneutrality. However, Sc, Y and parent materials can incorporate more oxygen vacancies leading to improved total conductivity and a greater TPB length. (Figure 3).

3.1.5. CO_2 stability

The issue of carbonate formation in BSCF materials at temperatures below 800°C in CO_2 containing atmospheres has been well documented [9,10]. To assess the influence of CO_2 on the electrode performance, EIS testing was carried out on both the parent composite (BSCF/GDC) and the Sc- substituted perovskite. The inlet gas used was composed of 5% CO_2 in air. Referring to Figure 6, the presence of CO_2 in the feed has a significant negative effect on the electrode performance which is shown by the 50% increase in polarization resistance. The Rp also varies with exposure time. When the feed is switched to air and the electrodes are no longer exposed to CO_2 the Rp of both the materials recovers in consecutive cycles. The EIS spectra allow for a better understanding of the effect of CO_2 on the ORR mechanism. As can be ascribed from the Nyquist and Bode plots (Figure 7), the introduction of CO_2 has a negligible effect on the high frequency resistances whereas at low to medium frequencies the resistance increases significantly. The LF and MF resistance change indicates a surface limitation process such as active site competition between CO_2 and O_2. LF processes have previously been associated with reactions involving adsorbed oxygen species which agrees with the competitive adsorption hypothesis. The MF resistances related to charge transfer reactions also increased in the CO_2 containing atmosphere indicating a TPB reduction due to blocking by the CO_2 adsorbed on the electrode.
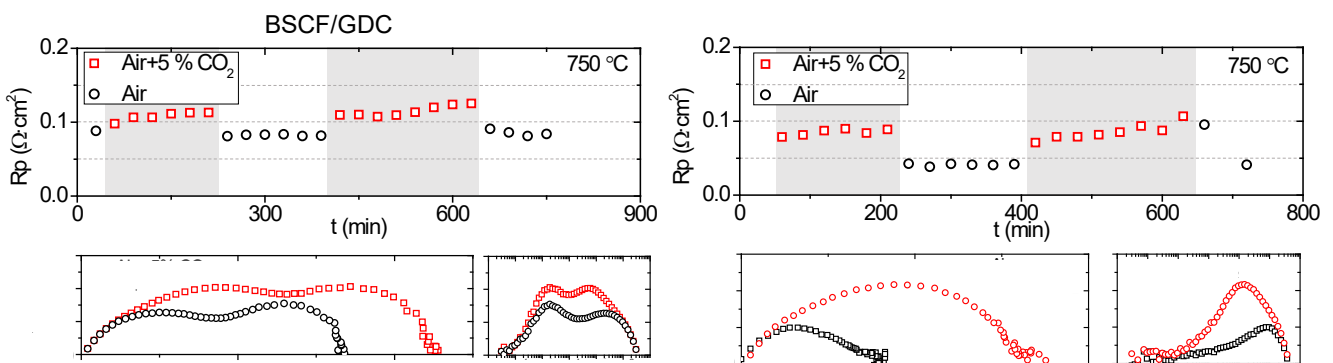

Figure 6. Influence of CO_2 containing atmosphere on the polarization resistance of (a) BSCF/GDC and (b) BSCFS/GDC. (c)/(e) Nyquist plot and (d)/(f) Bode plot in 5% of CO_2 and air for BSCF/GDC and BSCFS/GDC, respectively.

3.1.6. Fuel cell and electrolysis

For fuel cell and electrolysis mode measurements (Figure 7 (a)), a fully assembled cell was constructed based on the highest performing composite electrode (BSCFS/GDC) in the symmetric cell tests. Schematics of this cell being operated in both electrolysis and

fuel cell modes are depicted in Figure 7(a). In addition to the composite cathode, the cell consisted of an Ni-YSZ anode support provided by Forschungszentrum Jülich, an 8 mm thick YSZ electrolyte and a screen-printed GDC interlayer at the cathode-electrolyte interface, and cross-section image of the post-mortem sample is presented in Figure 7 (d)) As can be inferred from the image, the cell consists of a fully dense YSZ electrolyte, and porous GDC interlayer. The porosity of both electrodes was quite open to allow the mass transport and BSCFS/GDC electrode exhibited good adherence and no signs of delamination was observed after the electrochemical test.

The initial tests performed were to evaluate the performance of the BSCF/GDC electrode as a cathode in fuel cell mode. Electrochemical measurements were taken as the anode and cathode were respectively fed with wet H_2 (2.5% vol H_2O) and air. Under these feed conditions the maximum power density was measured at the following temperatures; 700,650,600 and 550 °C with 877, 538, 282 and 123 mW/cm^2 being the respectively obtained power density values (Figure 7 (c)). The open circuit voltage (OCV) was found to be 1.08 V at 700 °C and 1.14 V at 550 °C. These OCV values indicate that the fuel cell is properly sealed. In a previous study, a power density of ≈200 mW/cm^2 was achieved for a similar cell employing a similar BSFC/GDC composite electrode [42]. Dey et. al, reported a maximum power density of 180 mW/cm^2 at 750 °C using the same cell configuration as in this study ($Ba_{0.6}Sr_{0.4}Co_{0.8}Fe_{0.2}O_{3-\delta}$-GDC/GDC/YSZ/Ni-YSZ) [43]. In another work, The A-site of perovskite was substituted with Ba and Sr at an excess ratio of 1.03 and tested as a single-phase cathode on a Samarium doped Ceria (SDC) electrolyte. The resulting power density of 856.57 mW/cm^2 at 600°C was higher than the that which was obtained in this work [16]. Duan *et. al* conducted a study on how the sintering temperature of the GDC interlayer effects the performance of the BSCF electrode [12]. They found that 1250 °C was the optimum sintering temperatures and resulted in power densities of 810 and 520 mW/cm^2 at 700 and 650 °C respectively. Indicating that these values are slightly lower than those obtained in the present work.
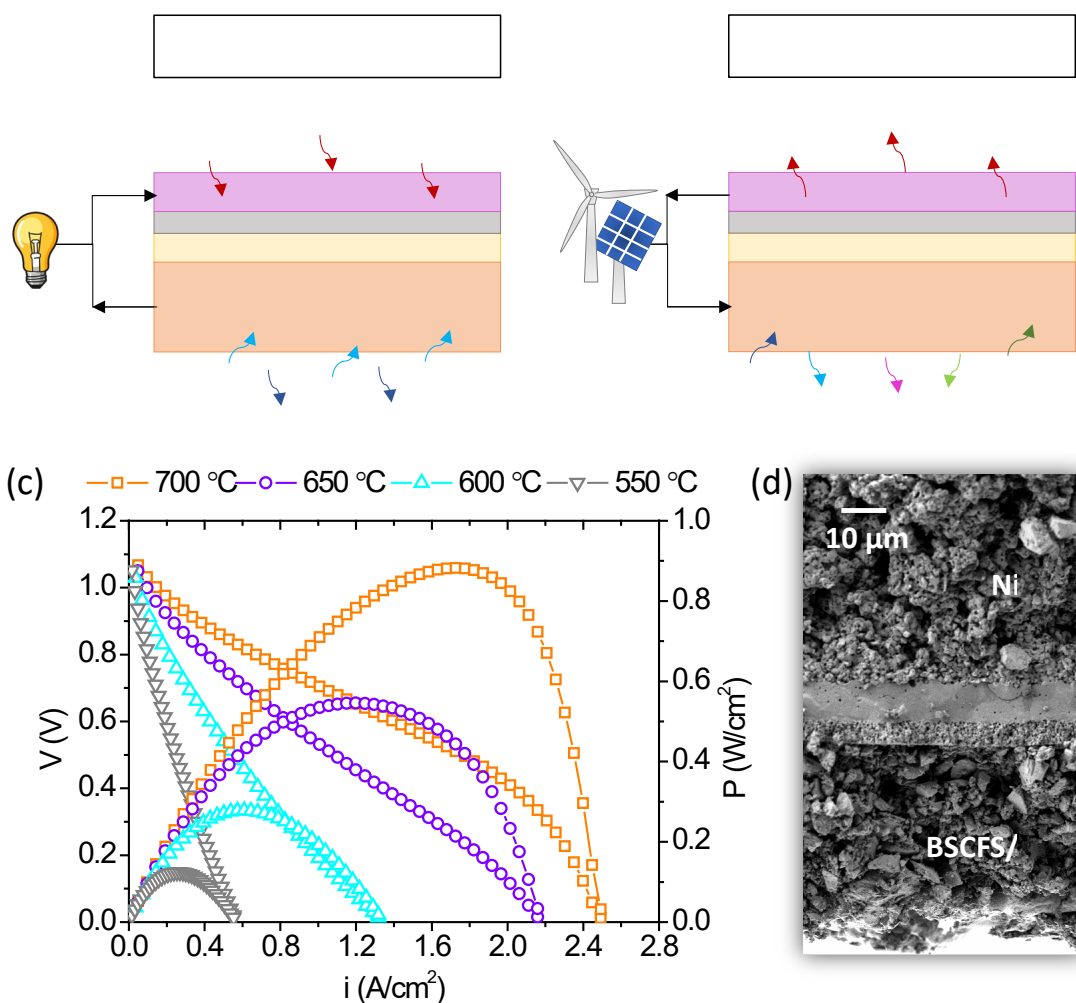
Figure 7. Cell configuration in (a) fuel cell and (b) electrolysis mode, (c) i-P and i-V curves of the Ni-YSZ/YSZ/GDC/(BSFCS/GDC) at different temperatures working with wet H_2 (2.5 % vol. H_2O) in the anode and air in the cathode and (d) SEM image with secondary electrons detector of electrochemical cell cross section.

To demonstrate the fully assembled cell's reversibility, tests involving the electrolysis and co-electrolysis of H_2O and/or CO_2 were carried out. The electrolysis experiments were performed at three different temperatures, 700, 600 and 500 °C. A continuous flow of 100 ml/min of wet argon with 2.5% vol. of H_2O was supplied to the cathode and a diverse range of current densities were applied for 30 minutes. The production of H_2 was quantified and detected using a gas chromatograph and mass spectrometer. The cell overpotentials at each set of conditions was recorded and are depicted in Figure 8 (a). H_2 is produced and detected from low imposed current densities throughout the entire operation temperature range. (Figure 8 (d)). The observed hydrogen production during electrolysis mode operation was constant and is represented by a steady mass spectrometer signal at all temperatures and current densities (Supporting Information, S3).

The measured voltages during electrolysis operation at different temperatures and current densities are plotted in Figure 8 (a). Three distinct regimes can be identified at low, medium and high current densities. For example, at 700 °C the highest activation energy is obtained when the cell operates at low current density. However, in the medium current range smaller i-V slopes are produced indicating a change in the electrolysis mechanism. When a current density above 200 mA/cm^2 is applied (high current regime), the voltage does not vary with current nor is the electroreduction voltage (2.3V) exceeded [44]. Similar behavior has been previously observed in YSZ electrolyte cells at high current densities and can be attributed to the promotion of electronic conductivity in the YSZ material [45].
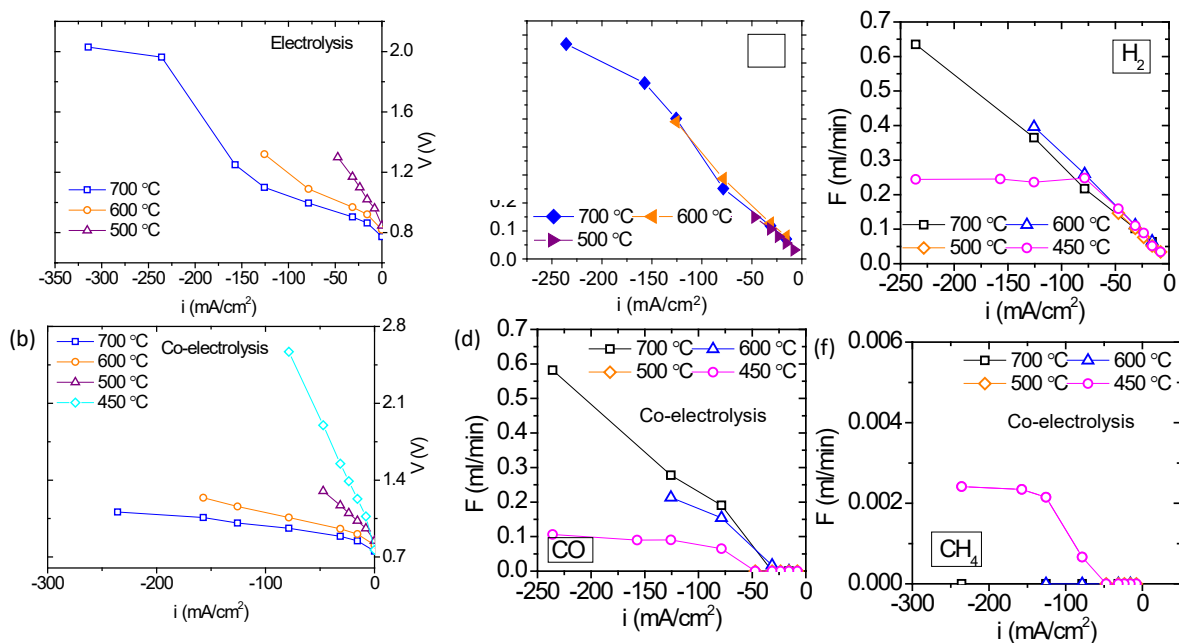

Figure 8. (a) Cell overpotential for the electrolysis and (b)co-electrolysis mode under different current densities. (c) Hydrogen production in electrolysis mode, (d) carbon monoxide. (e) hydrogen and (f) methane production working as a co-electrolyzer.
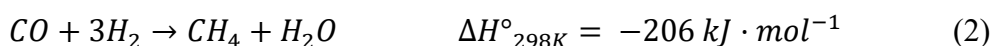
Finally, co-electrolysis operation to produce H$_2$ and CO was investigated. In these experiments, the cathode was still supplied with air while the Ni-YSZ anode was fed with a constant flow (100 mL/min) consisting of 10 ml/min of CO$_2$ and 2.5 % vol. H$_2$O with the remaining balance being Ar. Four different operation temperatures were selected for investigation. The obtained electrolysis products were detected and quantified via mass spectrometer (Supporting information, S4) and gas chromatograph (Figure 8d-f) analysis of the outlet gas. Co-electrolysis overpotential values were measured over a range of current densities and are shown in Figure 8 (b). As is observed in the Figure 8, the increase in cell resistance during low temperature operation results in higher voltages at the

corresponding current densities and lower Faraday's efficiencies for co-electrolysis and electrolysis mode (Supporting information S5). At the highest applied temperatures, the co-electrolysis operation produces lower cell voltages leading to superior cell efficiency [46,47]. The performed experiments revealed that the kinetics of the co-electrolysis process over the tested current density range are more favorable than those of electrolysis with only H_2O. Additionally, the activity shown by Ni for the high temperature electrochemical reduction of CO_2 is in agreement with previous findings [48].

The in-line gas analysis shows constant H_2 and CO generation over the entire measurement period for each selected current density. This consistent production is visually represented by the mass spectrometer signals for H_2, CO_2 and CO, which are 2,28 and 29 respectively (Supporting information, S4). The production of H_2 does not vary much over the temperature range at each applied current density. Since CO_2 electroreduction is happening simultaneously, the change in H_2 generation at different temperatures can be attributed to CO production and possible electronic leakage through the electrolyte. At low imposed currents (< 50 mA/cm^2) the presence of CO was not detected which confirms the high current density requirement for CO_2 electroreduction. When comparing the thermodynamics for CO_2 and H_2O reduction [49] it can be seen that at temperatures below 827 °C H_2O reduction is more favorable [46,48,50,51]. In addition to the electrochemical reactions, the Water Gas Shift Reaction ($CO + H_2O \rightarrow CO_2 + H_2$) and Reverse Water Gas Shift Reaction $CO_2 + H_2 \rightarrow CO + H_2O$) are also occurring at the electrodes. In the presence of hydrogen and at higher temperatures CO is formed via a combination of the kinetically rapid RWGS and CO_2 electrochemical reduction. However, at lower temperatures the WGRS begins to dominate such that high temperature operation is conducive to CO formation (Figure 8 (d)). This trend is reinforced by the kinetic and thermodynamic limitations of CO_2 electrochemical reduction at 500 °C and low current densities.

At 450°C the hydrogen generation behavior changes such that an increase in current density no longer leads to greater production of hydrogen at the cathode outlet gas. The mass spectrometer analysis differed from the low temperature analysis in that the mass signal ascribed to CH_4 was detected (Supporting Information, S4). The production of CH_4 comes at the cost of hydrogen generation and is thus responsible for the distinct low temperature behavior of the cell. At higher imposed current densities, the generation of

both CH_4 and CO is increased. Methane can be produced via two separate hydrogenation reactions, one based on CO and another on CO_2. However, the more agreed upon route to methane formation at these operation temperatures is that of CO in combination with the RWGS [52,53].

$$CO_2 + 4H_2 \rightarrow CH_4 + 2H_2O \qquad \Delta H°_{298K} = -165\ kJ \cdot mol^{-1} \qquad (1)$$
$$CO + 3H_2 \rightarrow CH_4 + H_2O \qquad \Delta H°_{298K} = -206\ kJ \cdot mol^{-1} \qquad (2)$$

4. Conclusion

In summary, several BSCF based cubic perovskite compounds were prepared by B-site substitution of the parent structure with Sc, Zr and Y and their electrochemical and stability properties were studied. The substituted materials showed superior stability in air and carbon dioxide containing atmospheres by reducing the formation of additional phases. Depending on the nature of the oxidation state and their effect on oxygen vacancy generation, the cations substituted had different effects on the polarization resistance. Sc exhibited the lowest resistance during the symmetrical cell tests due to its stability and its tendency to promote oxygen vacancy formation. The decreased electrode performance upon the introduction of CO_2 was attributed to a rise in low and medium frequency resistance which indicate surface process limitations due to active site blocking by adsorbed CO_2. The Sc- substituted material was chosen as the electrode for the full cell construction. The encouraging performance of the Sc substituted electrode in the fuel cell tests justify the promising nature of substituted BSCF materials for application in IT-SOFC cathodes. Furthermore, the composite electrode's favorable kinetics and low temperature methane generation during co-electrolysis operation is additional evidence for the potential sustainable application of the substituted perovskite material.

5. References

[1]   IEA. Global CO2 emissions in 2019. Glob CO2 Emiss 2019 2019.

[2]   Lobera MP, Balaguer M, García-Fayos J, Serra JM. Catalytic Oxide-Ion Conducting Materials for Surface Activation of Ba0.5Sr0.5Co0.8Fe0.2O3-δ Membranes. ChemistrySelect 2017;2:2949–55. https://doi.org/10.1002/slct.201700530.

[3]   Zhang Y, Knibbe R, Sunarso J, Zhong Y, Zhou W, Shao Z, et al. Recent Progress on Advanced Materials for Solid-Oxide Fuel Cells Operating Below 500 °C. Adv

Mater 2017;29. https://doi.org/10.1002/adma.201700132.

[4]   Huang Y, Ding J, Xia Y, Miao L, Li K, Zhang Q, et al. Ba0.5Sr0.5Co0.8-xFe0.2NbxO3-δ (x≤0.1) as cathode materials for intermediate temperature solid oxide fuel cells with an electron-blocking interlayer. Ceram Int 2020;46:10215–23. https://doi.org/10.1016/j.ceramint.2020.01.013.

[5]   Burriel M, Niedrig C, Menesklou W, Wagner SF, Santiso J, Ivers-Tiffée E. BSCF epitaxial thin films: Electrical transport and oxygen surface exchange. Solid State Ionics 2010;181:602–8. https://doi.org/10.1016/j.ssi.2010.03.005.

[6]   Sunarso J, Baumann S, Serra JM, Meulenberg WA, Liu S, Lin YS, et al. Mixed ionic-electronic conducting (MIEC) ceramic-based membranes for oxygen separation. J Memb Sci 2008;320:13–41. https://doi.org/10.1016/j.memsci.2008.03.074.

[7]   Wang S, Jin F, Li L, Li R, Qu B, He T. Stability, compatibility and performance improvement of SrCo0.8Fe0.1Nb0.1O3−Δ perovskite as a cathode for intermediate-temperature solid oxide fuel cells. Int J Hydrogen Energy 2017;42:4465–77. https://doi.org/10.1016/j.ijhydene.2016.11.015.

[8]   Shao Z, Haile SM. A high-performance cathode for the next generation of solid-oxide fuel cells. Nature 2004;431:170–3. https://doi.org/10.1038/nature02863.

[9]   Yan A, Cheng M, Dong Y, Yang W, Maragou V, Song S, et al. Investigation of a Ba0.5Sr0.5Co0.8Fe0.2O3- δ based cathode IT-SOFC. I. The effect of CO2 on the cell performance. Appl Catal B Environ 2006;66:64–71. https://doi.org/10.1016/j.apcatb.2006.02.021.

[10]   Scholten MJ, Schoonman J, van Miltenburg JC, Oonk HAJ. Synthesis of strontium and barium cerate and their reaction with carbon dioxide. Solid State Ionics 1993;61:83–91. https://doi.org/10.1016/0167-2738(93)90338-4.

[11]   Shannon R. Revised effective ionic radii and systematic studies of interatomic distances in halides and chalcogenides. Acta Crystallogr Sect A 1976;32:751–67.

[12]   Duan Z, Yang M, Yan A, Hou Z, Dong Y, Chong Y, et al. Ba0.5Sr0.5Co0.8Fe0.2O3- δ as a cathode for IT-SOFCs with a GDC interlayer. J Power Sources 2006;160:57–64. https://doi.org/10.1016/j.jpowsour.2006.01.092.

[13]   Murray EP, Barnett SA. La , Sr / MnO 3 – Ce , Gd / O 2yx composite cathodes for solid oxide fuel cells. Solid State Ionics 2001:265–73.

[14]   Qingshan Zhu, Tongan Jin, Yong Wang. Thermal expansion behavior and chemical compatibility of BaxSr1-xCo1-yFeyO3-δ with 8YSZ and 20GDC. Solid

State Ionics 2006;177:1199–204. https://doi.org/10.1016/j.ssi.2006.04.029.

[15] Shao Z, Yang W, Cong Y, Dong H, Tong J, Xiong G. Investigation of the permeation behavior and stability of a Ba0.5Sr0.5Co0.8Fe0.2O3−δ oxygen membrane. J Memb Sci 2000;172:177–88. https://doi.org/https://doi.org/10.1016/S0376-7388(00)00337-9.

[16] Zhou W, Ran R, Shao Z, Zhuang W, Jia J, Gu H, et al. Barium- and strontium-enriched (Ba0.5Sr0.5)1+xCo0.8Fe0.2O3-δ oxides as high-performance cathodes for intermediate-temperature solid-oxide fuel cells. Acta Mater 2008;56:2687–98. https://doi.org/10.1016/j.actamat.2008.02.002.

[17] Niedrig C, Taufall S, Burriel M, Menesklou W, Wagner SF, Baumann S, et al. Thermal stability of the cubic phase in Ba0.5Sr 0.5Co0.8Fe0.2O3 - δ (BSCF)1. Solid State Ionics 2011;197:25–31. https://doi.org/10.1016/j.ssi.2011.06.010.

[18] Efimov K, Xu Q, Feldhoff A. Transmission electron microscopy study of Ba0.5Sr 0.5Co0.8Fe0.2O3-δ perovskite decomposition at intermediate temperatures. Chem Mater 2010;22:5866–75. https://doi.org/10.1021/cm101745v.

[19] Mueller DN, De Souza RA, Weirich TE, Roehrens D, Mayer J, Martin M. A kinetic study of the decomposition of the cubic perovskite-type oxide BaxSr1-xCo0.8Fe0.2O 3-δ (BSCF) (x = 0.1 and 0.5). Phys Chem Chem Phys 2010;12:10320–8. https://doi.org/10.1039/c0cp00004c.

[20] Yakovlev S, Yoo C-Y, Fang S, Bouwmeester HJM. Phase transformation and oxygen equilibration kinetics of pure and Zr-doped Ba0.5 Sr0.5 Co0.8 Fe0.2 O 3-δ perovskite oxide probed by electrical conductivity relaxation. Appl Phys Lett 2010;96. https://doi.org/10.1063/1.3455908.

[21] Wang F, Igarashi K, Nakamura T, Yashiro K, Mizusaki J, Amezawa K. Tailoring the chemical stability of cobalt-rich perovskite mixed conductor. Solid State Ionics 2016;288:2–5. https://doi.org/10.1016/j.ssi.2016.01.018.

[22] Babakhani EG, Towfighi J, Shirazi L, Nakhaeipour A, Zamaniyan A, Shafiei Z. Structure Stability and Oxygen Permeability of Perovskite-type Oxides of Ba 0.5Sr 0.5Co 0.8Fe 0.1R 0.1O 3-δ (R=Al, Mn, Fe, Ce, Cr, Ni, Co). J Mater Sci Technol 2012;28:177–83. https://doi.org/10.1016/S1005-0302(12)60039-5.

[23] Porras-Vazquez JM, Slater PR. Synthesis of oxyanion-doped barium strontium cobalt ferrites: Stabilization of the cubic perovskite and enhancement in conductivity. J Power Sources 2012;209:180–3. https://doi.org/10.1016/j.jpowsour.2012.02.105.

[24] Kwak C, Jung DW, Yeon D-H, Kim JS, Park HJ, Ahn S-J, et al. Stabilization of high-cobalt-content perovskites for use as cathodes in solid oxide fuel cells. RSC Adv 2013;3:10669–72. https://doi.org/10.1039/c3ra41145a.

[25] Fang SM, Yoo C-Y, Bouwmeester HJM. Performance and stability of niobium-substituted $Ba0.5Sr0.5Co0.8Fe0.2O_3 - \delta$ membranes. Solid State Ionics 2011;195:1–6. https://doi.org/10.1016/j.ssi.2011.05.022.

[26] Maitra S, Chakrabarty N, Pramanik J. Decomposition kinetics of alkaline earth carbonates by integral approximation method. Cerâmica 2008;54:268–72. https://doi.org/10.1590/S0366-69132008000300001.

[27] Jung J Il, Misture ST, Edwards DD. The electronic conductivity of $Ba0.5Sr0.5Co_xFe_{1-x}O_{3-\delta}$ (BSCF:x=õ1.0) under different oxygen partial pressures. J Electroceramics 2010;24:261–9. https://doi.org/10.1007/s10832-009-9567-x.

[28] Jung J Il, Misture ST, Edwards DD. Oxygen stoichiometry, electrical conductivity, and thermopower measurements of BSCF ($Ba0.5Sr0.5Co_xFe_{1-X}O_{3-\delta}$, $0 \leq x \leq 0.8$) in air. Solid State Ionics 2010;181:1287–93. https://doi.org/10.1016/j.ssi.2010.06.033.

[29] Wang WG, Mogensen M. High-performance lanthanum-ferrite-based cathode for SOFC. Solid State Ionics 2005;176:457–62. https://doi.org/10.1016/j.ssi.2004.09.007.

[30] Adler SB. Factors governing oxygen reduction in solid oxide fuel cell cathodes. Chem Rev 2004;104:4791–843. https://doi.org/10.1021/cr020724o.

[31] Setevich C, Prado F, Caneiro A. Electrochemical response of several cathode configurations prepared with $Ba0.5Sr0.5Co0.8Fe0.2O_{3-\delta}$ and $Ce0.9Gd0.1O1.95$ for IT-SOFC. J Solid State Electrochem 2016;20:1633–43. https://doi.org/10.1007/s10008-016-3172-0.

[32] Murray EP, Tsai T, Barnett SA. Oxygen transfer processes in $(La,Sr)MnO_3/Y_2O_3$-stabilized ZrO_2 cathodes: An impedance spectroscopy study. Solid State Ionics 1998;110:235–43.

[33] Philippeau B, Mauvy F, Nicollet C, Fourcade S, Grenier JC. Oxygen reduction reaction in $Pr2NiO_{4+\delta}/Ce0.9Gd0.1O1.95$ and $La0.6Sr0.4Co0.2Fe0.8O_{3-\delta}$ $La0.8Sr0.2Ga0.8Mg0.2i$. J Solid State Electrochem 2015;19:871–82. https://doi.org/10.1007/s10008-014-2686-6.

[34] Haworth PF, Smart S, Serra JM, Diniz Da Costa JC. Combined investigation of

bulk diffusion and surface exchange parameters of silver catalyst coated yttrium-doped BSCF membranes. Phys Chem Chem Phys 2012;14:9104–11. https://doi.org/10.1039/c2cp41226h.

[35]   Yoo C-Y. Phase stability and oxygen transport properties of mixed ionic-electronic conducting oxides. 2012.

[36]   Dusastre V, Kilner JA. Optimisation of composite cathodes for intermediate temperature SOFC applications. Solid State Ionics 1999;126:163–74. https://doi.org/10.1016/S0167-2738(99)00108-3.

[37]   Baumann FS, Fleig J, Habermeier HU, Maier J. Ba0.5Sr0.5Co0.8Fe0.2O3-δ thin film microelectrodes investigated by impedance spectroscopy. Solid State Ionics 2006;177:3187–91. https://doi.org/10.1016/j.ssi.2006.07.057.

[38]   Nielsen J, Jacobsen T, Wandel M. Impedance of porous IT-SOFC LSCF:CGO composite cathodes. Electrochim Acta 2011;56:7963–74. https://doi.org/10.1016/j.electacta.2011.05.042.

[39]   Peng R, Wu T, Liu W, Liu X, Meng G. Cathode processes and materials for solid oxide fuel cells with proton conductors as electrolytes. J Mater Chem 2010;20:6218–25. https://doi.org/10.1039/C0JM00350F.

[40]   Kim J-D, Kim G-D, Moon J-W, Park Y-I, Lee W-H, Kobayashi K, et al. Characterization of LSM-YSZ composite electrode by ac impedance spectroscopy. Solid State Ionics 2001;143:379–89. https://doi.org/10.1016/S0167-2738(01)00877-3.

[41]   Jørgensen MJ, Mogensen M. Impedance of Solid Oxide Fuel Cell LSM/YSZ Composite Cathodes. J Electrochem Soc 2001;148. https://doi.org/10.1149/1.1360203.

[42]   Chang Y-C, Lee M-C, Kao W-X, Wang C-H, Lin T-N, Chang J-C. Fabrication and evaluation of electrochemical characteristics of the composite cathode layers for the anode-supported solid-oxide fuel cells. J Taiwan Inst Chem Eng 2011;42:775–82. https://doi.org/https://doi.org/10.1016/j.jtice.2011.01.004.

[43]   Dey S, Mukhopadhyay J, Lenka RK, Patro PK, Sharma A Das, Mahata T, et al. Synthesis and characterization of Nanocrystalline Ba0·6Sr0·4Co0·8Fe0·2O3 for application as an efficient anode in solid oxide electrolyser cell. Int J Hydrogen Energy 2020;45:3995–4007. https://doi.org/10.1016/j.ijhydene.2019.12.083.

[44]   Weppner W. Formation of intermetallic Pt-Zr compounds between Pt electrodes and ZrO2-based electrolytes, and the decomposition voltage of yttria-doped ZrO2.

J Electroanal Chem 1977;84:339–50. https://doi.org/10.1016/S0022-0728(77)80384-7.

[45] Laguna-Bercero MA, Campana R, Larrea A, Kilner JA, Orera VM. Performance and aging of microtubular YSZ-based solid oxide regenerative fuel cells. Fuel Cells 2011;11:116–23. https://doi.org/10.1002/fuce.201000069.

[46] Zhan Z, Kobsiriphat W, Wilson JR, Pillai M, Kim I, Barnett SA. Syngas production by coelectrolysis of CO <inf>2</inf>/H <inf>2</inf>O: The basis for a renewable energy cycle. Energy and Fuels 2009;23:3089–96. https://doi.org/10.1021/ef900111f.

[47] Graves C, Ebbesen SD, Mogensen M. Co-electrolysis of CO2 and H2O in solid oxide cells: Performance and durability. Solid State Ionics, vol. 192, 2011, p. 398–403. https://doi.org/10.1016/j.ssi.2010.06.014.

[48] Zhan Z, Zhao L. Electrochemical reduction of CO2 in solid oxide electrolysis cells. J Power Sources 2010;195:7250–4. https://doi.org/10.1016/j.jpowsour.2010.05.037.

[49] Graves C, Ebbesen SD, Mogensen M, Lackner KS. Sustainable hydrocarbon fuels by recycling CO2 and H 2O with renewable or nuclear energy. Renew Sustain Energy Rev 2011;15:1–23. https://doi.org/10.1016/j.rser.2010.07.014.

[50] Stoots CM, O'Brien JE, Herring JS, Hartvigsen JJ. Syngas production via high-temperature coelectrolysis of steam and carbon dioxide. J Fuel Cell Sci Technol 2009;6:0110141–01101412. https://doi.org/10.1115/1.2971061.

[51] Gaudillere C, Navarrete L, Serra JM. Syngas production at intermediate temperature through H2O and CO2 electrolysis with a Cu-based solid oxide electrolyzer cell. Int J Hydrogen Energy 2014;39. https://doi.org/10.1016/j.ijhydene.2013.12.045.

[52] Navarro JC, Centeno MA, Laguna OH, Odriozola JA. Policies and motivations for the CO2 valorization through the sabatier reaction using structured catalysts. A review of the most recent advances. Catalysts 2018;8. https://doi.org/10.3390/catal8120578.

[53] Jürgensen L, Ehimen EA, Born J, Holm-Nielsen JB. Dynamic biogas upgrading based on the Sabatier process: Thermodynamic and dynamic process simulation. Bioresour Technol 2015;178:323–9. https://doi.org/https://doi.org/10.1016/j.biortech.2014.10.069.